BIOTECHINTELLECT, 2026, 3(1) e22 (1-18)
https://jbiotechintel.com/index.php/biotechintel

Research Article

eISSN: 3115-7920

OPEN ACCESS

# In Silico Exploration of Zerumbone Interactions with DNA Damage Response Protein Domains: Relevance to Breast Cancer

**Zahra Sanaimehr[1], Nasim Forghani[2], Nima Ghahremani Nezhad[3*], Ahmed Issa Al-Tameemi[4]**

[1]Department of Chemistry, Faculty of Science, Universiti Putra Malaysia, 43400 UPM Serdang, Selangor, Malaysia.
[2]Department of Biology, Faculty of Basic Sciences and Engineering, Gonbad Kavous University, Gonbad Kavous, Golestan, Iran.
[3]Institute of Systems Biology (INBIOSIS), Universiti Kebangsaan Malaysia 43600 UKM Bangi, Selangor Malaysia
[4]College of Dentistry, Al-Iraqi University, 10053 Al-Adhamiya, Baghdad, Iraq

**Article history:**
Received 18 July 2026
Revised 19 Sep 2026
Accepted 22 Sep 2026
Published online 25 Sep 2026

**Keywords:** Breast Cancer, Zerumbone, Molecular Docking, Molecular Dynamics Simulations, DNA Damage

How to cite this article:
Sanaimehr Z, Forghani N, Ghahremani Nezhad N, Al-Tameemi AI, In silico exploration of zerumbone interactions with DNA damage response protein domains: relevance to breast cancer, BiotechIntellect, 2026; 3(1): e22, 1-18.

https://doi.org/10.66224/BiotechIntellect.3.1.60

***corresponding author's**
Nima Ghahremani Nezhad,

Email:

nimanezhad@ukm.edu.my

© 2026 the authors. This is an open access article under the terms of the Creative Commons Attribution-NonCommercial 4.0 International (CC BY-NC 4.0) License.

## ABSTRACT

**Background and Objective:** Breast cancer remains a major cause of cancer-related mortality among women, with tumor heterogeneity and therapeutic resistance presenting significant challenges to treatment. The DNA damage response (DDR) pathway is essential for DNA repair and may contribute to cancer cell survival and treatment resistance, making DDR-associated proteins potential therapeutic targets. This study investigated the potential interactions of zerumbone, a bioactive compound derived from *Zingiber zerumbet*, with DDR-related proteins using molecular docking, molecular dynamics (MD) simulations, and molecular mechanics Poisson–Boltzmann surface area (MM/PBSA) analysis.

**Materials and Methods:** Molecular docking of 12 DDR-related protein structures identified favorable predicted interactions, with docking scores ranging from −5.24 to −6.69 kcal/mol. Five complexes with the most favorable docking scores were selected for three independent 100-ns MD simulations.

**Results and Conclusion:** Root-mean-square deviation and fluctuation (RMSD & RMSF) analyses revealed differences in global structural deviations and residue-level flexibility, with 3JVE–zerumbone exhibiting relatively low RMSD values and 7CMZ–zerumbone showing greater structural fluctuations. Radius of gyration analyses indicated that overall structural compactness remained relatively consistent during the simulations, while principal component analysis revealed comparatively restricted conformational sampling for 3JVE–zerumbone and broader conformational exploration for 7CMZ–zerumbone. MM/PBSA calculations, performed without an entropy term, yielded estimated binding energies ranging from −8.20 to −26.53 kcal/mol, with 7CMZ–zerumbone and 3AL2–zerumbone exhibiting the most favorable estimates. Notably, 3JVE–zerumbone displayed relatively low RMSD values but the least favorable MM/PBSA estimate, illustrating that limited structural deviation does not necessarily correspond to more favorable estimated binding energetics. Collectively, these findings provide structural and energetic insights into the predicted interactions of zerumbone with DDR-related protein domains and identify candidate complexes for further investigation.

***What is "already known":***

- Rhizosphere-associated *Streptomyces* spp. represent promising sources of antimicrobial compounds.
- Antimicrobial activity depends on isolates and target microorganisms, highlighting the importance of screening strains against a diverse panel of pathogens.

| | |
|---|---|
| ***What this article adds:*** | • Antimicrobial activity of actinomycetes isolated from the rhizospheres of rosemary (*Salvia rosmarinus*) and spearmint (*Mentha spicata*).<br>• Molecular identification revealed selected isolates were related to *Streptomyces amritsarensis* and *Streptomyces antibioticus*.<br>• Isolates show distinct antimicrobial profiles: broad inhibitory activity by RR1 & high activity of MR4 against methicillin-susceptible and methicillin-resistant *S. aureus*. |

## 1. INTRODUCTION

Cancer continues to be a critical global health concern, with projections indicating a substantial rise in both incidence and mortality rates over the coming decades. According to the World Health Organization (WHO), nearly 35 million new cases of cancer and over 16 million related deaths are anticipated annually by 2050 [1]. Breast cancer, in particular, accounts for a considerable portion of this burden, affecting millions of women worldwide [2]. A wide array of treatments is available for cancer, including surgical procedures, chemotherapy, radiation therapy, immunotherapy, hormone therapy, and targeted approaches that address specific cancer pathways. Advanced methods, such as gene therapy and personalized medicine, are now being developed to align with the genetic profiles of individual patients [3]. However, despite these advancements, many newer targeted therapies have limitations, including high costs, nonspecific toxicities, and suboptimal effectiveness [4]. A significant challenge with anticancer medications is their lack of selectivity, which often results in damage to healthy tissues and organs [5]. Moreover, both conventional chemotherapy and targeted therapies are frequently associated with the emergence of resistance [6]. This resistance can develop through mechanisms such as genetic mutations or the activation of alternative biological pathways, reducing the long-term success of these treatments.

The DNA Damage Response (DDR) pathway is an intricate signaling network that detects, signals, and repairs DNA damage, ensuring the genomic stability of cells. This pathway enables cancer cells to repair therapy-induced DNA damage efficiently, thereby enhancing their survival under therapeutic stress and contributing significantly to treatment resistance [7]. Targeting the DDR pathway has emerged as a potential strategy to counteract this resistance and improve therapeutic outcomes [8,9]. Key proteins involved in the DDR pathway serve as promising therapeutic targets. For instance, mediator of DNA damage checkpoint protein 1 (MDC1) plays a pivotal role in recruiting repair proteins to sites of DNA double-strand breaks and activating cellular checkpoints [10]. Inhibiting MDC1 may overcome resistance in cancers heavily reliant on DDR for survival, such as triple-negative breast cancer, ovarian cancer, and non-small cell lung cancer [11]. Similarly, Neighbour of BRCA1 gene NBR1, which regulates selective autophagy, is crucial for managing cellular stress and damaged organelles. Blocking NBR1-mediated autophagy could enhance the efficacy of DNA-damaging therapies like chemotherapy and radiation by increasing the accumulation of damaged organelles and promoting cancer cell death [12,13]. Another critical player in the DDR pathway is BRCA1, which is involved in homologous recombination repair and acts as a key tumor suppressor by maintaining genomic stability [14]. While directly inhibiting BRCA1 does not prevent cancer, it creates a vulnerable state in cancer cells, making them more responsive to targeted therapies such as PARP inhibitors and DNA-damaging agents [15]. This approach selectively eliminates cancer cells with BRCA1 deficiencies or a high dependency on DDR mechanisms, thereby halting tumor progression. TopBP1 (Topoisomerase II Binding Protein 1) is another significant regulator within the DDR and replication stress response. It plays a dual role in suppressing tumor growth and contributing to therapy resistance. Inhibiting TopBP1 sensitizes cancer cells to DNA-damaging therapies, making it a valuable target for tumors characterized by high replication stress or dependence on DDR pathways [16,17]. RPA-70N (Replication Protein A 70 kDa N-terminal domain), a subunit of the Replication Protein A complex, is essential for maintaining genomic stability during DNA replication. Although it supports normal cellular functions, cancer cells exploit RPA70N to survive high replication stress and therapy-induced damage. Targeting RPA70N offers a novel therapeutic

This open-access article distributed under the terms of the Creative Commons Attribution Non Commercial 4.0 License (CC BY-NC 4.0).
To view a copy of this license, visit http://creativecommons.org/licenses/by/4.0/

approach, especially when combined with other DNA-damaging agents or DDR-targeting therapies, to selectively impair cancer cell survival [18,19]. Collectively, these DDR proteins represent critical therapeutic targets. By impairing their repair functions using inhibitors or compounds, it is possible to sensitize cancer cells to DNA-damaging therapies and reduce their survival mechanisms. This strategy enhances the effectiveness of treatments such as chemotherapy and radiation, potentially leading to improved clinical outcomes. Natural products have consistently been a rich source of therapeutic agents, particularly in cancer treatment, due to their effective pharmacological properties and reduced side effects compared to synthetic alternatives [20–22]. One such compound, zerumbone, a bioactive sesquiterpene derived from the rhizomes of *Zingiber zerumbet*, has attracted attention for its wide range of biomedical benefits. These include antioxidant, antibacterial, antipyretic, antinociceptive, anti-inflammatory, hepatoprotective, and immunomodulatory effects [23–25]. Beyond these general health benefits, zerumbone exhibits significant antitumor activity by influencing key processes such as cell proliferation, angiogenesis, and programmed cell death, making it a subject of extensive research in oncology [26,27]. Zerumbone has shown great promise in targeting triple-negative breast cancer through its ability to modulate various molecular pathways. Zerumbone influences the Notch signaling pathway by increasing presenilin-1 protein levels, which facilitates the cleavage of Notch2. At the same time, it reduces the levels of cleaved Notch1 and Notch4, promoting programmed cell death and curbing the migration of cancer cells [28]. Furthermore, zerumbone inhibits NF-κB activity, leading to a reduction in IL-8 and MMP-3 production [29,30]. This, in turn, diminishes the cell migration and invasive behavior stimulated by IL-1β. It also causes cell cycle arrest at the G2/M phase and induces apoptosis through Bax/Bak pathways [31]. Moreover, zerumbone reduces the expression of CXCR4, thereby inhibiting cancer cell invasion and metastasis [32]. Another important mechanism involves its suppression of TGF-β1, which leads to reduced levels of fibronectin, MMP-2, and MMP-9 through decreased phosphorylation of Smad3. This, combined with its inhibition of Ki67 expression, significantly curtails tumor proliferation [33]. Animal studies using xenograft models have further demonstrated zerumbone's effectiveness in reducing tumor size, weight, and spread [31,33]. These findings underscore its potential as a treatment for triple-negative breast cancer, given its ability to combat tumor growth and metastasis effectively. Despite these well-documented anticancer effects, the role of zerumbone in targeting the DNA Damage Response (DDR) pathway remains relatively unexplored [34]. Investigating how zerumbone inter-acts with DDR proteins may provide new insights into its therapeutic potential, particularly in addressing treatment resistance in cancers with a high dependency on DDR mechanisms, such as triple-negative breast cancer.

Advances in molecular docking and molecular dynamics (MD) simulations, including the incurporation of enhanced sampling techniques and solvation models, have substantially improved the precision of predicting protein-ligand interactions [35,36]. These computational methods have become invaluable for identifying and refining compounds that selectively target components of the DDR pathway [37]. Recent investigations have utilized these approaches to study zerumbone's interaction with proteins implicated in cancer progression. For example, research has identified its binding affinity to multiple targets, including AKT1, XIAP, HSP90AA1, MDM2, and EP300, in breast cancer models, highlighting its potential to act on multiple molecular pathways. Other studies have demonstrated zerumbone's capability to engage with proteins involved in cellular stress response, apoptosis regulation, and metastatic processes [38–40]. Despite these findings, there remains a scarcity of studies directly examining zerumbone's influence on DDR-specific proteins. This gap underscores the need for further investigation into its therapeutic potential within DDR-targeted cancer treatments. To address this gap, the current study uses molecular docking and MD simulations to investigate the predicted interactions of zerumbone with selected DNA damage response (DDR)-related protein structures, including MDC1, NBR1, BARD1, TopBP1, Brc1, and RPA70N. The selected structures represent specific protein domains or constructs involved in DNA damage signaling, replication checkpoint control, and genome maintenance.



This open-access article distributed under the terms of the Creative Commons Attribution Non Commercial 4.0 License (CC BY-NC 4.0).
To view a copy of this license, visit http://creativecommons.org/licenses/by/4.0/

By evaluating zerumbone interactions across these targets, this study aims to provide computational insights into its potential interactions with DDR-associated proteins and identify candidate complexes for further investigation in the context of breast cancer.

## 2. MATERIALS AND METHODS

### 2.1. Preparation of protein and ligand structures

The high-resolution crystal structures of key proteins involved in DNA damage response and repair mechanisms were meticulously selected from the Protein Data Bank (PDB). The specific PDB entries used in this study include the BRCT Repeat Domain of MDC1 (PDB ID: 2ADO), PB1 Domain of NBR1 (PDB ID: 2BKF), MDC1 Tandem BRCT Domains (PDB ID: 2ETX), TopBP1 BRCT7/8 domains (PDB ID: 3AL2), BARD1 Ankyrin Repeat Domain (PDB ID: 3C5R), Sixth BRCT Domain of TopBP1 (PDB IDs: 3JVE and 3PD7), TopBP1 BRCT4/5 domains (PDB ID: 3UEN), Brc1 BRCT5-BRCT6 domains (PDB ID: 3L40), BARD1 BRCT (PDB ID: 6M14), BRCT7/8 (PDB ID: 7CMZ), and RPA70N (PDB ID: 8K00). These structures were retrieved via the RCSB PDB database (http://www.rcsb.org). In cases where the PDB structures contained missing residues, these gaps were carefully filled using loop modelling to restore the full integrity of the protein. Following the completion of the structure, energy minimization was performed to optimize the repaired regions and the overall protein conformation by 10,000 steps using the steepest descent minimization algorithm. The CHARMM force field in Discovery Studio 2016 (Accelrys, Inc., San Diego, CA, USA) was employed to achieve the lowest energy states, thereby ensuring that the proteins were in a stable conformation suitable for docking. For ligand preparation, the bioactive compound zerumbone was acquired from the PubChem database (https://pubchem.ncbi.nlm.nih.gov/) [41]. The 3D structure of zerumbone was then subjected to energy minimization to achieve an energetically favorable conformation, enhancing its interaction potential with the target proteins. The structural characteristics and biological relevance of the 12 protein targets investigated in this study are summarized in Table 1.

### 2.2. Site-specific molecular docking

The protein and ligand structures were prepared for docking using AutoDock Tools [42]. Protein structures were imported, with hydrogens added and partial charges assigned. Active site grids were precisely defined, and the structures were converted to pdbqt format. The grid centers were x = 37.84, y = 1.00 and z = 3.14 for 2ADO, x = 8.72, y = 76.19 and z = 3.45 for 2BKF, x = 37.70, y = 0.98 and z = 3.26 for 2ETX, x = 15.65, y = 27.89 and z = 18.58 for 3AL2, x = 1.84, y = 15.17 and z = 18.42 for 3C5R, x = 9.19, y = 72.78 and z = 10.09 for 3JVE, x = -7.87, y = 12.23 and z = -13.27 for 3L40, x = 18.88, y = 18.57 and z = 29.21 for 3PD7, x = -0.40, y = 49.41 and z = 76.82 for 3UEN, x = 18.17, y = 2.16 and z = 25.12 for 6M14, x = 2.56, y = -4.73 and z = 17.58 for 7CMZ and x = -7.38, y = -7.96 and z = 10.93 for 8K00 PDB files, respectively. For all targets, the docking grid dimensions were set to 50 × 50 × 50 Å. The docking search used an exhaustiveness value of 8 and an energy range of 4 kcal/mol. The previously energy-minimized ligand, zerumbone, was loaded into AutoDock Tools, where Gasteiger charges were computed, polar hydrogens were added, rotatable bonds were detected, and the structure was saved in pdbqt format. Docking was then executed with AutoDock Vina using an exhaustiveness of 8 and an energy range of 4 kcal/mol, and the binding conformations with the lowest binding free energy (most negative affinity, kcal/mol) were selected for analysis. After docking, protein-ligand complexes exhibiting the most negative binding energies were constructed using UCSF Chimera (version 1.18) [43]. These complexes were then analyzed using Discovery Studio, where the key interactions between zerumbone and the protein targets were visualized.

### 2.3. Molecular dynamics (MD) simulations

Following the docking analysis, five protein–ligand complexes (7CMZ, 3AL2, 3UEN, 3JVE, and 6M14) were selected from the 12 screened targets based on their five most favorable predicted docking scores for MD simulations using GROMACS v2022.6 [44], employing the AMBER99SB forcefield [45].

This open-access article distributed under the terms of the Creative Commons Attribution Non Commercial 4.0 License (CC BY-NC 4.0).
To view a copy of this license, visit http://creativecommons.org/licenses/by/4.0/

**Table 1.** Structural characteristics and biological relevance of the protein targets selected for molecular docking.

| Number | PDB† ID | Protein and domain/construct | Functional relevance |
|---|---|---|---|
| **1** | 2ADO | Mediator of DNA MDC1‡, tandem BRCT repeats | The tandem BRCT repeats recognize the phosphorylated C-terminal tail of H2AX (γ-H2AX), contributing to the recognition and repair of DNA double-strand breaks |
| **2** | 2ETX | Mediator of DNA MDC1, tandem BRCT domains | The structure comprises the tandem BRCT domains of MDC1, while microcephalin (MCPH1) is implicated in DNA damage checkpoint signaling, DNA repair, and transcription. |
| **3** | 2BKF | Neighbor of BRCA1 gene, PB1 domain | The PB1 domain mediates protein–protein interactions with titin kinase and the scaffold protein p62. |
| **4** | 3UEN | DNA topoisomerase 2-binding protein 1 (TopBP1), tandem BRCT4/5 domains | BRCT5 recognizes phosphorylated SDT repeats of MDC1, contributing to TopBP1 recruitment to γ-H2AX-associated foci and DNA replication checkpoint signaling. |
| **5** | 3JVE | DNA topoisomerase 2-binding protein 1 (TopBP1), BRCT6 domain | BRCT6 is implicated in interactions with E2F1 and poly(ADP-ribose) polymerase 1 (PARP1). Structural and binding studies suggest that it does not independently function as a phosphopeptide-binding domain. |
| **6** | 3PD7 | Human TopBP1, sixth BRCT domain | Crystal structure of the sixth BRCT domain of human TopBP1 (DNA topoisomerase 2-binding protein 1). |
| **7** | 3AL2 | DNA topoisomerase 2-binding protein 1 (TopBP1), tandem BRCT7/8 domains | BRCT7/8 recognizes a phosphorylated motif in BACH1/FANCJ, contributing to DNA replication checkpoint activation at stalled replication forks. |
| **8** | 7CMZ | TopBP1, tandem BRCT7/8 domains in complex with the APS motif of PHF8 | PHF8-mediated demethylation of TopBP1 contributes to ATR activation and the cellular response to replication stress. |
| **9** | 3C5R | BRCA1-associated RING domain protein 1 (BARD1), ankyrin-repeat domain | BARD1 is the constitutive nuclear partner of BRCA1. The BRCA1–BARD1 complex contributes to genomic stability through DNA damage signaling and repair, transcriptional regulation, and cell-cycle control. |
| **10** | 6M14 | BARD1 BRCT domain carrying the V695L mutation | The V695L mutation affects the BARD1–OLA1 interaction and reduces BARD1-mediated activation of OLA1 ATPase activity. |
| **11** | 3L40 | *Schizosaccharomyces pombe* Brc1, tandem BRCT5–BRCT6 domains | Brc1 binds phosphorylated H2A (γH2A) and contributes to genome integrity during S phase and DNA damage responses associated with replication. |
| **12** | 8K00 | Human RPA70N–MRE11 fusion construct | RPA70N, the N-terminal domain of the RPA70 subunit, interacts with multiple DNA damage response proteins. The associated study investigates the structural basis of these interactions. |

† Protein Data Bank, ‡ damage checkpoint protein 1

The ligand topologies were generated using the Antechamber module [46] integrated into the Amber package, with partial charges assigned via the AM1-BCC model [47], then converted to GROMACS format using the Acpype code. Each simulation system was placed within a cubic simulation box, solvated with SPC water molecules [48]. Counter ions replaced enough water molecules to neutralize the system. Periodic boundary conditions (PBC) were applied in all three dimensions. Energy minimization was initially conducted using the steepest descent algorithm [49]. Subsequent equilibration was performed under constant volume (NVT) conditions for 100 ps at 300 K, with a coupling constant of 0.1 ps, utilizing the Berendsen thermostat [50]. This was followed by a constant pressure equilibration phase, conducted at 1 bar for 1 ns with a coupling constant of 5.0 ps, maintained by the Parrinello-Rahman barostat [51]. To constrain rigid water molecules and hydrogen bonds, SETTLE [52] and LINCS [53] algorithms were used to constrain the geometry of water molecules and the appropriate bond lengths, respectively. The Particle Mesh Ewald (PME) method was used for the accurate calculation of long-range Coulombic (electrostatic) interactions [54]. For van der Waals interactions, a Lennard-Jones potential with a cutoff method was applied [55]. The cutoff distance for both Coulombic and van der Waals

This open-access article distributed under the terms of the Creative Commons Attribution Non Commercial 4.0 License (CC BY-NC 4.0). To view a copy of this license, visit http://creativecommons.org/licenses/by/4.0

interactions was set to 12 Å. To minimize artifacts, van der Waals interactions were smoothly truncated using a switch function between 10 Å and 12 Å, ensuring a continuous potential and avoiding discontinuities at the cutoff distance. Each complex was subjected to three independent MD simulations, each with a production duration of 100 ns and an integration time step of 2 fs. The resulting data were analyzed using Visual MD (VMD) [56] and Discovery Studio (DS). Structural behavior was assessed using root-mean-square deviation (RMSD), root-mean-square fluctuation (RMSF), and radius of gyration (Rg). Principal component analysis (PCA) was also performed to characterize the conformational dynamics of the protein–ligand complexes.

### 2.4. MM/PBSA binding free energy calculations

To estimate the binding free energies of various protein-ligand complexes, the gmx_MMPBSA tool was utilized [57]. For each complex, three independent 100 ns MD trajectories were analyzed, with snapshots extracted from the production phase at 100 ps intervals, yielding approximately 1,000 snapshots per trajectory and 3,000 snapshots per complex across the three replicates. The binding energy was estimated using the standard MM/PBSA of Eq. 1:

$$\Delta G_{binding} = \Delta G_{complex} - \Delta G_{protein} - \Delta G_{ligand} \quad \text{Eq. 1}$$

where ΔG_complex, ΔG_protein, and ΔG_ligand represent the energy contributions of the protein–ligand complex, protein, and ligand, respectively. Each energy term was approximated by Eq. 2:

$$G_{system} \approx \Delta E_{MM} + \Delta G_{solvation} \quad \text{Eq. 2}$$

The molecular mechanics energy (ΔE_MM) comprises bonded and non-bonded interactions, including electrostatic and van der Waals interactions. The solvation free energy (ΔG_solvation) consists of polar and non-polar contributions. Polar solvation was calculated using the Poisson–Boltzmann equation, while the non-polar contribution was estimated from the solvent-accessible surface area (SASA). Entropic contributions (−TΔS) were not calculated; therefore, the resulting entropy-excluded energy estimates were used for relative comparisons between complexes rather than as absolute thermodynamic binding free energies [58].

### 2.5. Statistical analysis

All computational analyses were independently performed in triplicate. Data processing and statistical analyses were carried out using GraphPad Prism version 9 (GraphPad Software, Inc., CA, USA). Statistical significance was determined by one-way analysis of variance (ANOVA), followed by Tukey's multiple comparison post hoc test. A *P* value of less than 0.05 was considered statistically significant. Data are expressed as mean ± standard deviation (SD).

## 3. RESULTS AND DISCUSSION

### 3.1. Molecular docking analyses

Molecular docking studies were conducted to examine the binding interactions between the bioactive compound zerumbone and various proteins involved in DNA damage response and repair mechanisms. The docking simulations were performed using AutoDock Vina, and the results are summarized in Table 2, which presents the binding affinity of zerumbone with the selected proteins. The negative binding energy values suggest favorable interactions between zerumbone and the target proteins, with lower energy values indicating favorable docking scores. Among the analyzed proteins, the most favorable binding energy was observed for the BRCT7/8 domains (PDB ID: 7CMZ), with a binding energy of -6.69 kcal/mol. Detailed analysis of the docking pose (Figure 1A) revealed several key interactions contributing to this favorable docking score. Zerumbone forms hydrophobic interactions with residues such as Leu1319, Leu1414, Phe1411, and Ala1470, which contribute to the stabilization of the protein-ligand complex. While hydrophobic interactions are common, their significance in this context arises from their location

This open-access article distributed under the terms of the Creative Commons Attribution Non Commercial 4.0 License (CC BY-NC 4.0). To view a copy of this license, visit http://creativecommons.org/licenses/by/4.0/

within the hydrophobic binding pocket, which enhances the ligand's stability and affinity by minimizing solvent exposure and favorably interacting with nonpolar regions of the protein.

In the TopBP1 BRCT7/8 domains (PDB ID: 3AL2), zerumbone exhibited a notable binding affinity with an energy of -6.547 kcal/mol (Figure 1B). Similar hydrophobic interactions were observed with Leu1319, Leu1414, Phe1411, and Ala1470, which were further stabilized by a hydrogen bond with Arg1407. The presence of a well-defined hydrophobic pocket is known to facilitate the tight binding of hydrophobic ligands, like zerumbone, by minimizing solvent exposure and maximizing interaction with nonpolar residues in the binding site [59]. This favorable environment likely contributes to the observed lower binding energies, consistent with other studies that highlight the importance of hydrophobic pockets in ligand binding and stability [59,60]. The interaction with the BRCT4/5 domains (PDB ID: 3UEN) showed a binding affinity of -6.510 kcal/mol (Figure 1C). In this docking pose, zerumbone forms hydrophobic interactions with several key residues, including Phe563, Pro597, Leu598, and Leu599. Additionally, two hydrophobic interactions with Phe666 and a hydrogen bond with Ser663 further contribute to the binding stability. The alignment of zerumbone within the hydrophobic pocket of the BRCT4/5 domains highlights its potential to interact effectively with multiple sites, forming an extensive network of ligand-protein contacts that collectively stabilize the complex.

For the Sixth BRCT Domain of TopBP1 (PDB ID: 3JVE), zerumbone showed a binding energy of -6.128 kcal/mol (Figure 1D). Although the hydrophobic pocket in this domain appears less pronounced compared to the other BRCT domains, the binding is significantly stabilized by hydrogen bonds with Lys915 and Gly949, along with a hydrophobic interaction with Lys915. This suggests that while hydrophobic interactions are less dominant in this complex, the specific placement of hydrogen bonds compensates, resulting in a relatively stable interaction. Finally, zerumbone's interaction with the BARD1 BRCT domain (PDB ID: 6M14) demonstrated a binding affinity of -5.870 kcal/mol (Figure 1E). In this binding pose, zerumbone establishes several hydrophobic interactions with key residues such as Leu622, Lys693, and Ala697. Additionally, a significant hydrogen bond is formed between Ser602 and zerumbone, adding to the stability of the complex. The relatively less negative binding energy, in this case, suggests that while the hydrophobic pocket in this domain is present, it is less optimal compared to other BRCT domains, leading to slightly reduced stability of the protein-ligand complex.

Across all the analyzed interactions, a clear pattern emerges: the presence of well-defined hydrophobic pockets and zerumbone's ability to engage in multiple hydrophobic interactions are key factors driving higher binding affinities. This indicates that zerumbone has a strong affinity for binding within hydrophobic environments, which are prevalent in BRCT domains involved in DNA repair pathways. The slight variations in binding affinities among the different BRCT domains suggest that while hydrophobic interactions are crucial, the exact positioning and accessibility of these hydrophobic residues, as well as the potential for additional hydrogen bonding, play a significant role in determining the overall strength of the protein-ligand interaction. The docking results of this study are consistent with previous research on zerumbone's interactions with various protein targets. Singh et al. demonstrated that zerumbone binds effectively to TNF-alpha by forming strong hydrophobic interactions and hydrogen bonds within its active site, highlighting its broad potential for interacting with different proteins [61]. Similarly, in our study, zerumbone exhibited favorable binding to the BRCT7/8 domains of TopBP1, with a binding affinity of -6.69 kcal/mol. These results suggest that zerumbone can effectively interact with various protein targets, not only by leveraging hydrophobic interactions but also by forming hydrogen bonds, making it a versatile compound for different biological pathways and targets, including TNF-alpha and TopBP1.

This open-access article distributed under the terms of the Creative Commons Attribution Non Commercial 4.0 License (CC BY-NC 4.0). To view a copy of this license, visit http://creativecommons.org/licenses/by/4.0

**Table 2.** Molecular docking scores of zerumbone against the 12 selected protein targets.

| Receptor (PDB† ID) | Binding Energy (kcal/mol) |
|---|---|
| 7CMZ | -6.69 |
| 3AL2 | -6.547 |
| 3UEN | -6.51 |
| 3JVE | -6.128 |
| 6M14 | -5.87 |
| 3PD7 | -5.851 |
| 2ETX | -5.774 |
| 3L40 | -5.571 |
| 2BKF | -5.44 |
| 2ADO | -5.42 |
| 8K00 | -5.266 |
| 3C5R | -5.238 |

† Protein Data Bank

## 3.2. Molecular dynamics (MD) simulations analyses

### 3.2.1. RMSD analyses

The RMSD profiles of the protein–zerumbone (ZRB) complexes describe their time-dependent structural deviations from the reference structures during the 100 ns simulations. RMSD values reflect the degree of structural deviation from a reference structure during MD simulations. Generally, relatively low and stable RMSD values indicate that a protein maintains its overall structure with limited conformational changes, whereas higher values or substantial fluctuations may indicate greater structural flexibility or conformational rearrangement [62]. Starting with the 3AL2-ZRB complex (Figure 2, black line), the RMSD values indicate a generally stable behavior, with the RMSD fluctuating between 0.20 and 0.25 nm for most of the simulation. However, a slight increase in RMSD towards the end of the simulation, reaching up to 0.30 nm, suggests some degree of flexibility or structural adjustment within the complex over time. Despite these fluctuations, the RMSD remained within a relatively narrow range for most of the simulation, indicating limited global structural deviation in the 3AL2-ZRB complex during the sampled trajectory. The 3JVE-ZRB complex (Figure 2, red line) shows a slightly lower RMSD range compared to 3AL2, with values generally hovering around 0.15 to 0.20 nm.

The lower RMSD range of 3JVE-ZRB compared with 3AL2-ZRB indicates smaller global structural deviations during the simulation. The relatively low and consistent RMSD values indicate that the 3JVE-ZRB complex underwent comparatively small global structural deviations throughout the sampled trajectory. For the 3UEN-ZRB complex (Figure 2, green line), the RMSD trajectory indicates slightly higher fluctuations, with values ranging from 0.20 to 0.30 nm. The 3UEN-ZRB complex displayed RMSD fluctuations comparable to those of 3AL2-ZRB, with a somewhat broader range of structural deviations than observed for 3JVE-ZRB. The RMSD profile of 6M14-ZRB (Figure 2, blue line) increased from approximately 0.20 nm to around 0.25 nm and then approached a plateau, suggesting an initial structural adjustment followed by comparatively limited changes in global structural deviation. Lastly, the 7CMZ-ZRB complex (Figure 2, yellow line) exhibits the highest RMSD values among all the complexes, fluctuating between 0.25 and 0.35 nm throughout the simulation. The higher RMSD values of 7CMZ-ZRB indicate greater global structural deviations during the simulation than those observed for the other complexes.

### 3.2.2. RMSF analyses

The RMSF (Root Mean Square Fluctuation) data provide additional insights into the flexibility of individual residues within the protein-ligand complexes throughout the simulation [63]. RMSF analysis identifies regions of a protein that exhibit greater residue-level fluctuations during MD simulations, providing insights into local flexibility and the dynamic behavior of the protein structure [64]. The 3AL2-ZRB complex (Figure 3, black line) exhibits relatively low fluctuations throughout most of the protein, with only a few regions showing higher RMSF values, particularly towards the C-terminal end.

This open-access article distributed under the terms of the Creative Commons Attribution Non Commercial 4.0 License (CC BY-NC 4.0).
To view a copy of this license, visit http://creativecommons.org/licenses/by/4.0/

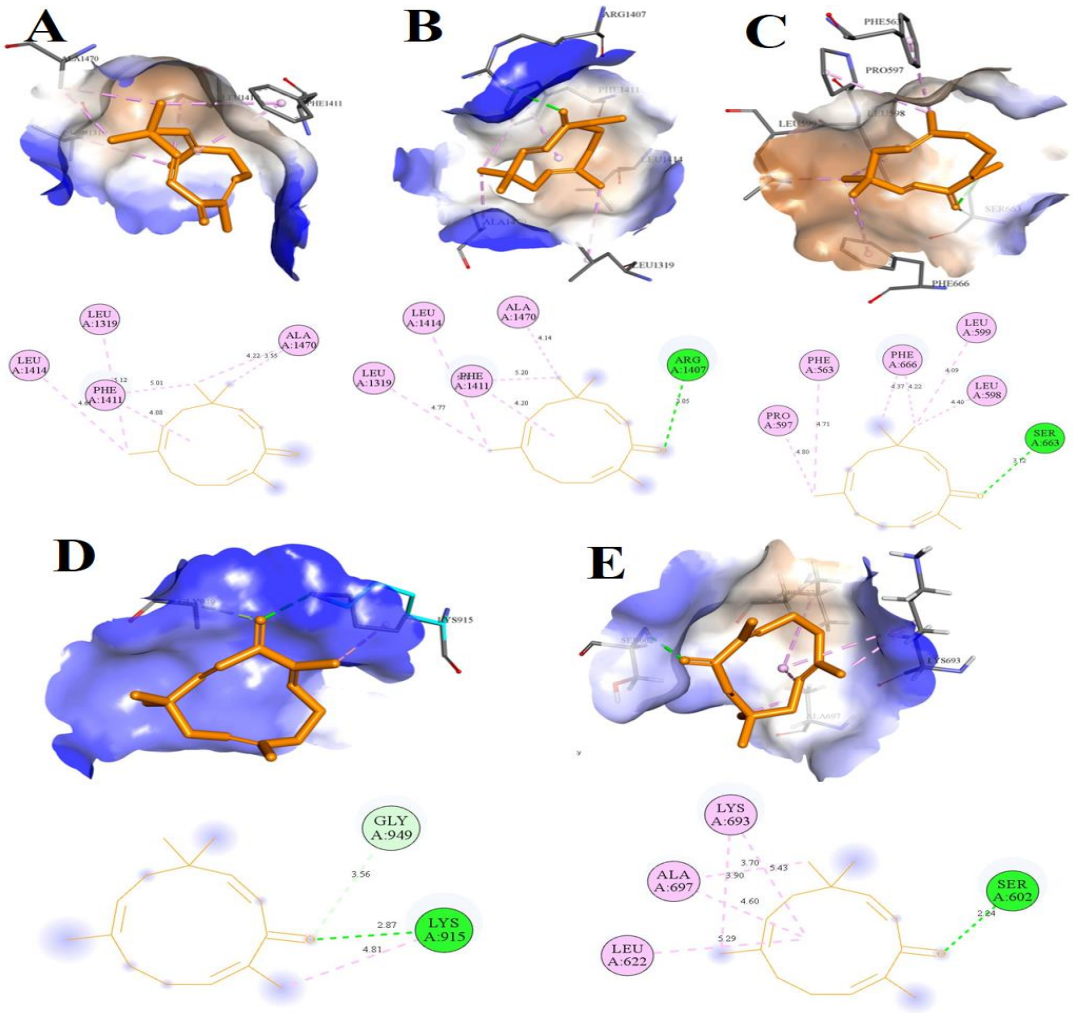



**Figure 1.** Docking pose and interactions of Zerumbone with target proteins. **(A)** Molecular interactions between the 7CMZ protein and zerumbone. **(B)** Molecular interactions between the 3AL2 protein and zerumbone. **(C)** Molecular interactions between the 3UEN protein and zerumbone. **(D)** Molecular interactions between the 3JVE protein and zerumbone. **(E)** Molecular interactions between the 6M14 protein and zerumbone.

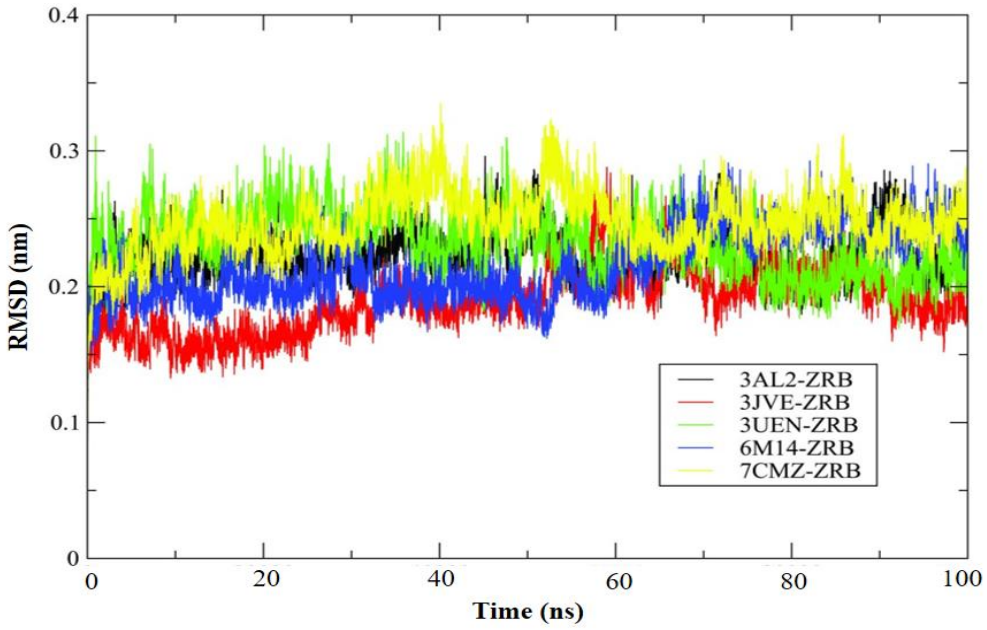



**Figure 2.** Root-mean-square deviation (RMSD) profiles of the zerumbone–protein complexes during the 100-ns molecular dynamics simulations. The 3JVE–ZRB complex exhibited comparatively low RMSD values, indicating smaller global structural deviations, whereas the 7CMZ–ZRB complex showed higher RMSD values, reflecting greater structural deviations during the simulations.

Commercial 4.0 License (CC BY-NC 4.0).

This suggests that the majority of the protein remains stable, with only specific loops or terminal regions experiencing flexibility. The 3JVE-ZRB complex (Figure 3, red line) shows a similar trend, with generally low RMSF values, indicating a comparatively stable protein structure with limited residue-level fluctuations. However, certain regions, likely corresponding to loops or unstructured regions, exhibit higher fluctuations, which is common in proteins and often does not impact the overall stability of the complex. In contrast, the 3UEN-ZRB complex (Figure 3, green line) presents higher RMSF values across several regions, indicating that this complex experiences more significant conformational changes during the simulation. This is particularly evident in the terminal regions and certain loop regions, which are more prone to movement [65]. This increased flexibility may correlate with the slightly higher RMSD values observed in this complex, suggesting that while the complex is generally stable, certain regions are more flexible [66]. The 6M14-ZRB complex (Figure 3, blue line) also shows moderate RMSF values, with fluctuations concentrated in specific regions. The fluctuations in this complex suggest some flexibility, particularly in areas that may not be directly involved in the binding interface, allowing the complex to adapt while maintaining overall stability. The 7CMZ-ZRB complex (Figure 3, yellow line) shows the highest RMSF values among all the complexes, particularly in the loop regions and terminal ends. A comparison of the RMSF results with the RMSD data reveals a clear pattern that aligns with and supports the initial observations. Complexes with lower RMSD values, such as 3JVE-ZRB, generally show lower RMSF values, indicating a comparatively stable protein structure with limited residue-level fluctuations. In contrast, complexes like 7CMZ-ZRB, which exhibited higher RMSD values, also show higher RMSF fluctuations, highlighting the relationship between residue flexibility and overall complex stability. These findings reinforce the conclusions drawn from the RMSD analysis and the docking studies. The RMSF profiles reveal differences in residue-level flexibility among the protein–zerumbone complexes, with lower fluctuations indicating more restricted local movements and higher fluctuations reflecting greater flexibility in specific protein regions.

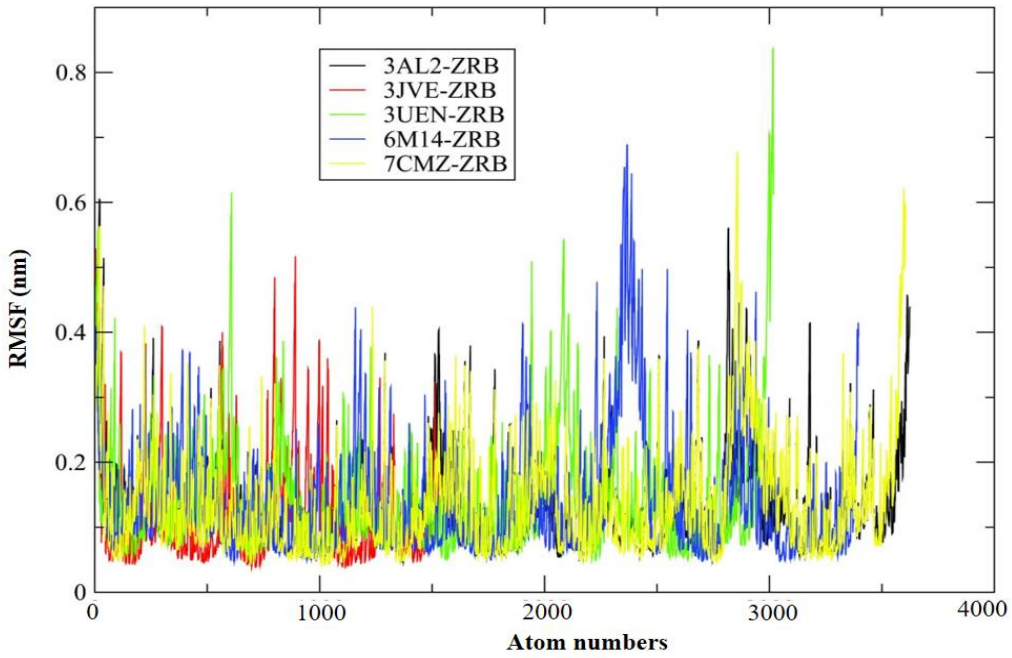



**Figure 3.** Root-mean-square fluctuation profiles of the zerumbone–protein complexes, showing residue-level fluctuations during the molecular dynamics simulations. The 3JVE–ZRB complex exhibited generally lower fluctuations across much of the structure, whereas the 7 CMZ–ZRB complex showed higher fluctuations in several regions, particu-larly in loops and terminal regions.

This open-access article distributed under the terms of the Creative Commons Attribution Non Commercial 4.0 License (CC BY-NC 4.0).
To view a copy of this license, visit http://creativecommons.org/licenses/by/4.0/

### 3.2.3. Radius of Gyration (Rg) analyses

A relatively stable radius of gyration (Rg) throughout a MD simulation indicates that the protein maintains a consistent overall compactness, whereas substantial changes in Rg may reflect structural expansion or compaction during the simulation [67]. For the 3AL2-ZRB complex (Figure 4, black line), the Rg fluctuates around 2.0 nm, with minor variations throughout the simulation. This relatively narrow range suggests that the overall compactness of the 3AL2-ZRB complex remains largely unchanged during the simulation, with no substantial expansion or compaction evident from the Rg profile. The 3JVE-ZRB complex (Figure 4, red line) exhibited an Rg of approximately 1.3 nm, which remained relatively constant throughout the simulation, indicating consistent overall compactness. The 3JVE and 7CMZ protein structures contained 104 and 237 residues, respectively. Therefore, the substantially lower Rg of 3JVE-ZRB is likely attributable, at least in part, to the smaller size of the protein construct. The 3UEN-ZRB complex (Figure 4, green line) showed modest Rg fluctuations between approximately 1.9 and 2.0 nm, suggesting that its overall compactness remained largely unchanged during the simulation. Similarly, the 6M14-ZRB complex (Figure 4, blue line) exhibited relatively consistent Rg values, ranging from approximately 1.93 to 2.03 nm. These limited variations indicate that neither complex underwent substantial changes in overall compactness during the sampled trajectories, although local residue-level fluctuations may still occur.

The 7CMZ-ZRB complex (Figure 4, yellow line) displayed Rg values of approximately 1.95–2.0 nm, comparable to those of 3UEN-ZRB and 6M14-ZRB. Despite some fluctuations, its Rg profile suggests that the overall compactness of the complex remained relatively consistent throughout the simulation. Although 7CMZ-ZRB exhibited higher RMSD and RMSF values in the previous analyses, these observations reflect global structural deviations and local residue flexibility, respectively, and do not necessarily indicate substantial changes in overall compactness. Overall, the Rg profiles suggest that all five complexes—3AL2-ZRB, 3JVE-ZRB, 3UEN-ZRB, 6M14-ZRB, and 7CMZ-ZRB—maintained relatively consistent overall compactness during the simulations. Because Rg depends on protein size and shape, differences in absolute Rg values among the complexes partly reflect differences in their structural characteristics.

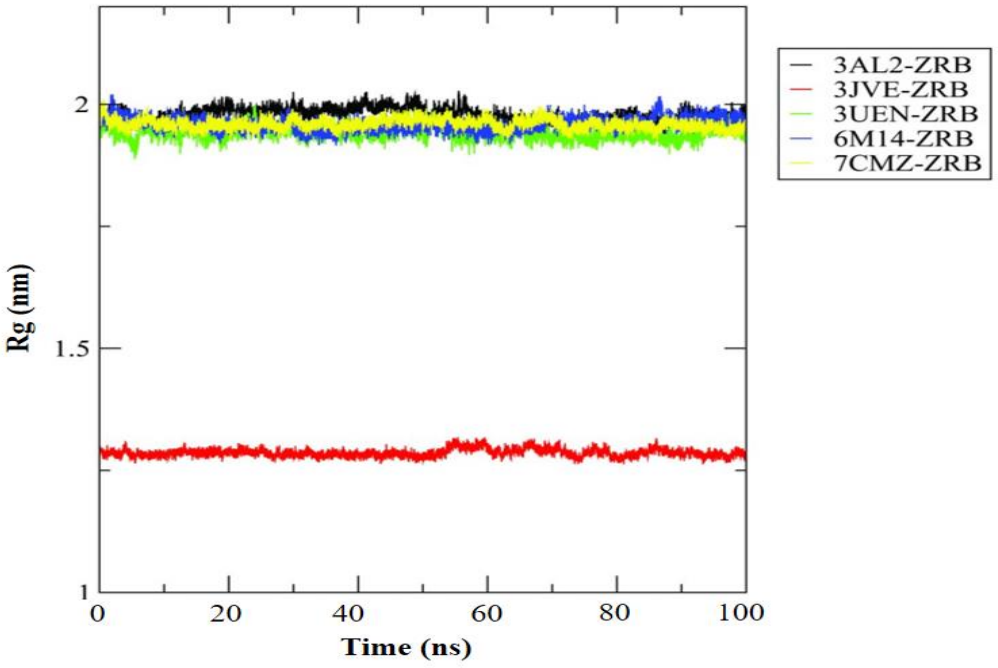



**Figure 4.** Radius of gyration (Rg) profiles of the zerumbone–protein complexes during the 100-ns molecular dynamics simulations. The Rg profiles remained relatively consistent throughout the simulations, suggesting that the overall compactness of each protein structure was generally maintained. The Rg values differed among the complexes, partly reflecting differences in protein size and structural characteristics.

This open-access article distributed under the terms of the Creative Commons Attribution Non Commercial 4.0 License (CC BY-NC 4.0). To view a copy of this license, visit http://creativecommons.org/licenses/by/4.0

### 3.2.4. Principal component analyses (PCA)

Principal component analysis (PCA) is a statistical method used in MD simulations to reduce the dimensionality of complex datasets and identify the dominant collective motions of biomolecular systems [35]. By projecting protein–ligand trajectories onto the first two principal components derived from the covariance matrix of atomic displacements, PCA provides a two-dimensional representation of the conformational space sampled during a simulation. This approach helps characterize differences in conformational sampling and collective structural motions among protein–ligand complexes [36].

In this study, PCA revealed differences in the conformational spaces sampled by the five protein–zerumbone (ZRB) complexes. The 3AL2-ZRB complex (Figure 5, black) exhibited a moderate spread in the PCA projection, indicating a degree of conformational variability during the simulation. This observation is broadly consistent with its intermediate RMSD values and relatively stable Rg profile, suggesting that the complex underwent structural fluctuations while maintaining relatively consistent overall compactness. The 3JVE-ZRB complex (Figure 5, red) displayed more compact clustering in the two-dimensional PCA projection, indicating a narrower range of sampled conformations along the first two principal components. This observation is consistent with the relatively low RMSD values observed for this complex. Overall, the PCA results suggest comparatively restricted conformational sampling for 3JVE-ZRB during the simulated trajectory.

The 3UEN-ZRB complex (Figure 5, green) also exhibited conformational sampling across the PCA projection, reflecting structural variability during the simulation. Together with its moderate RMSD values and relatively consistent Rg profile, this pattern suggests that the complex underwent conformational fluctuations without substantial changes in overall compactness. The 6M14-ZRB complex (Figure 5, blue) showed clustering across multiple regions of the PCA projection, suggesting that the trajectory sampled different conformational regions along the first two principal components. This distribution may reflect transitions between conformations during the simulation. Finally, the 7CMZ-ZRB complex (Figure 5, yellow) exhibited the broadest distribution in the PCA projection, indicating more extensive conformational sampling along the first two principal components. This observation is consistent with the higher RMSD and RMSF values reported for this complex, which indicate greater global structural deviations and local residue-level fluctuations, respectively. Overall, PCA revealed distinct conformational behaviors among the five protein–ZRB complexes, ranging from relatively restricted sampling in 3JVE-ZRB to broader conformational exploration in 7CMZ-ZRB. These results complement the RMSD, RMSF, and Rg analyses by providing information about collective motions and the conformational space sampled during the simulations. Together, these metrics characterize different aspects of protein structural dynamics and should be interpreted collectively when evaluating the behavior of the simulated complexes.

### 3.2.5. MM/PBSA binding free energy analysis and key residue contributions in protein-zerumbone complexes

To further characterize the interactions between zerumbone (ZRB) and the target proteins, MM/PBSA (Molecular Mechanics Poisson–Boltzmann Surface Area) calculations were performed using snapshots from the MD simulations. This analysis provided estimates of the binding energies of the protein–ligand complexes and identified key residues contributing to the calculated binding energies [68]. The MM/PBSA calculations revealed differences in the estimated binding energies (ΔTOTAL) among the five protein–ZRB complexes. The 7CMZ–ZRB complex exhibited the most favorable estimated binding energy (−26.53 kcal/mol), followed by 3AL2–ZRB (−21.02 kcal/mol), 3UEN–ZRB (−19.37 kcal/mol), 6M14–ZRB (−15.53 kcal/mol), and 3JVE–ZRB (−8.20 kcal/mol). These results indicate that 7CMZ–ZRB had the most favorable MM/PBSA energy estimate among the investigated complexes, followed by 3AL2–ZRB and 3UEN–ZRB.

This open-access article distributed under the terms of the Creative Commons Attribution Non Commercial 4.0 License (CC BY-NC 4.0). To view a copy of this license, visit http://creativecommons.org/licenses/by/4.0/

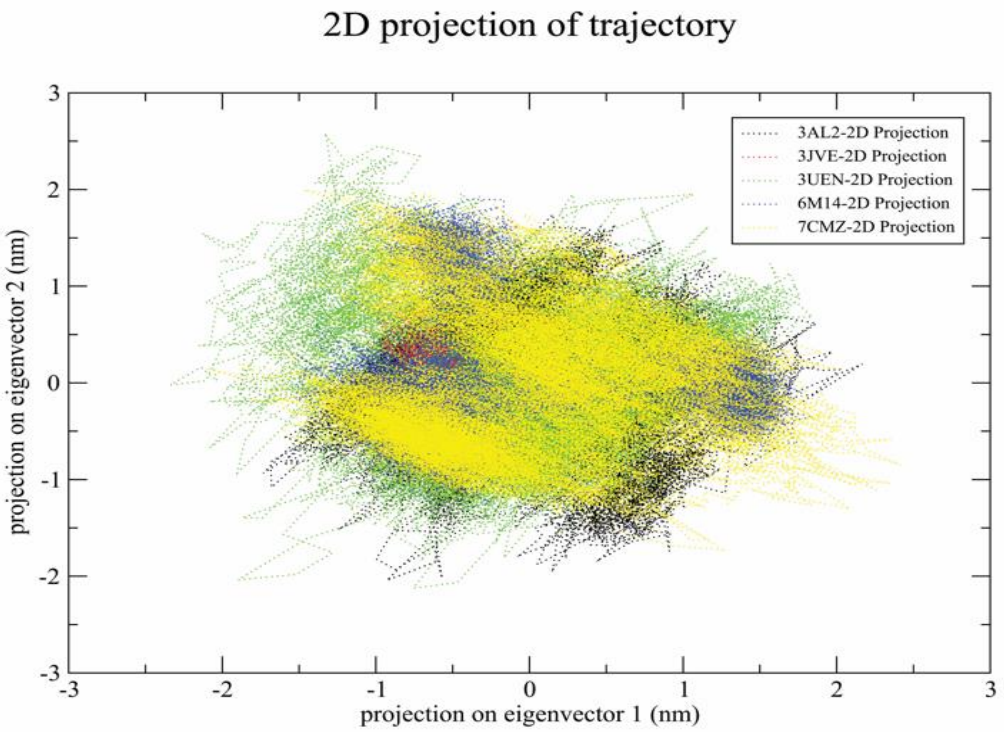



**Figure 5.** Principal component analysis (PCA) of the zerumbone–protein complexes, illustrating differences in conformational sampling during the molecular dynamics simulations. The 3JVE–ZRB complex exhibits a more compact distribution in the PCA projection, indicating a narrower range of sampled conformations, whereas the 7CMZ–ZRB complex shows a broader distribution, reflecting more extensive conformational sampling along the first two principal components.

The 6M14–ZRB complex showed an intermediate energetic profile, whereas 3JVE–ZRB had the least favorable estimated binding energy. The energetic ranking highlights 7CMZ–ZRB as a promising candidate for further investigation and demonstrates differences in the predicted interactions of zerumbone across the five target proteins.

Residue-level energy decomposition identified several residues that contributed notably to the calculated binding energies. In the 3AL2–ZRB complex, Phe1411 and Arg1407 were identified as important contributors (Figure 6A). In the 3JVE–ZRB complex, Phe938 showed a notable contribution (Figure 6B). Similarly, Phe666 contributed to the calculated binding energy of 3UEN–ZRB (Figure 6C), while Leu622 and Ala697 were identified as notable contributors in 6M14–ZRB (Figure 6D). In the 7CMZ–ZRB complex, Arg1407 and Phe1411 were among the residues contributing to the calculated binding energy (Figure 6E). These findings identify potential residue-level determinants of the predicted interactions between zerumbone and the target proteins.

Comparison of the docking results with the post-MD energy-decomposition analysis revealed overlap in the residues implicated in the predicted interactions. For example, Phe1411 was identified as a contributing residue in both the 3AL2–ZRB and 7CMZ–ZRB complexes. This consistency supports the potential importance of this residue in the predicted interactions of zerumbone with these protein targets. Overall, the MM/PBSA results complement the docking and structural-dynamics analyses by providing an energetic perspective on the five protein–ZRB complexes. Considering the favorable MM/PBSA estimate for 7CMZ–ZRB alongside its docking score, this complex emerged as a promising candidate for further investigation of zerumbone–protein interactions. Experimental studies can subsequently assess the binding interactions and determine their functional relevance.


This open-access article distributed under the terms of the Creative Commons Attribution Non Commercial 4.0 License (CC BY-NC 4.0).
To view a copy of this license, visit http://creativecommons.org/licenses/by/4.0

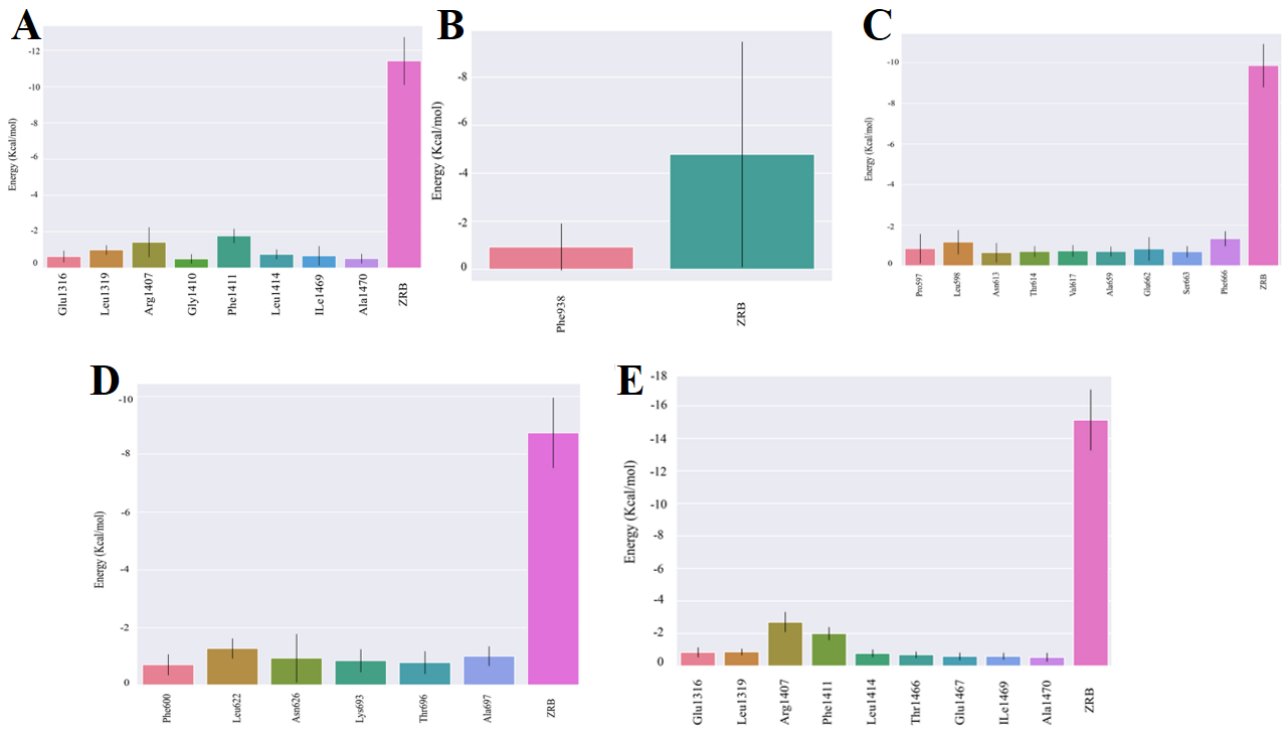



**Figure 6.** Binding free energy analysis using MM/PBSA calculations for Zerumbone (ZRB) interactions with various protein targets. **(A)** Binding energy contributions for ZRB with 3AL2. **(B)** Energy contributions for ZRB with 3JVE. **(C)** Interaction energies for ZRB with 3UEN. **(D)** MM/PBSA results for ZRB with 6M14. **(E)** Energy contribution for ZRB with 7CMZ. Error bars represent the standard deviation of calculated energies.

## 4. CONCLUSION

This study investigated the predicted interactions of zerumbone with multiple DNA damage response (DDR)-related protein structures using molecular docking, MD simulations, and MM/PBSA analysis. The selected targets included domains or constructs of MDC1, NBR1, BARD1, TopBP1, *Schizosaccharomyces pombe* Brc1, and RPA70N. The MD simulations revealed distinct structural-dynamic behaviors among the selected protein–zerumbone complexes, while MM/PBSA calculations provided complementary estimates of their binding energetics. In particular, the 7CMZ–zerumbone complex exhibited the most favorable docking score and MM/PBSA energy estimate among the five complexes selected for MD simulations. These findings provide computational insights into the predicted interactions of zerumbone with DDR-associated protein structures and identify candidate complexes for further investigation. Experimental studies are needed to determine whether these interactions influence protein function or DNA damage response activity. Further biochemical and cellular investigations, including studies in triple-negative breast cancer models, will be required to establish the biological significance and potential therapeutic relevance of these findings.

## 5. DECLARATIONS

### 5.1. Acknowledgements

.....

### 5. 2. Conflict of Interest

The authors declare that they have no known competing financial interests or personal relationships that could have appeared to influence the work reported in this paper.

### 5.3. Authors Contributions

ZS and NGN have conceived, designed, verified the data, and written the manuscript. NF and AIAT contributed to the literature review, manuscript revision, and editing of the text.

This open-access article distributed under the terms of the Creative Commons Attribution Non Commercial 4.0 License (CC BY-NC 4.0).
To view a copy of this license, visit http://creativecommons.org/licenses/by/4.0/

### 5.4. Ethics approval & Consent for publication

Not applicable.

### 5.5. Funding

This research did not receive any specific grant from funding agencies in the public, commercial, or not-for-profit sectors.

### 5.6. Data availability

All data generated or analyzed during this study are included in this published article.

## 6. REFERENCES

[1] F. Bray, M. Laversanne, H. Sung, J. Ferlay, R.L. Siegel, I. Soerjomataram, A. Jemal, Global cancer statistics 2022: GLOBOCAN estimates of incidence and mortality worldwide for 36 cancers in 185 countries, CA. Cancer J. Clin. 74 (2024) 229–263. https://doi.org/10.3322/caac.21834.

[2] M. Arnold, E. Morgan, H. Rumgay, A. Mafra, D. Singh, M. Laversanne, J. Vignat, J.R. Gralow, F. Cardoso, S. Siesling, I. Soerjomataram, Current and future burden of breast cancer: Global statistics for 2020 and 2040, Breast 66 (2022) 15–23. https://doi.org/10.1016/j.breast.2022.08.010.

[3] P.A. Williams, S.K. Zaidi, R. Sengupta, AACR Cancer Progress Report 2023: Advancing the Frontiers of Cancer Science and Medicine, Clin. Cancer Res. 29 (2023) 3850–3851. https://doi.org/10.1158/1078-0432.CCR-23-2591.

[4] M.T. Van Leeuwen, S. Luu, H. Gurney, M.R. Brown, S.A. Pearson, K. Webber, L. Hunt, S. Hong, G.P. Delaney, C.M. Vajdic, Cardiovascular toxicity of targeted therapies for cancer: An overview of systematic reviews, JNCI Cancer Spectr. 4 (2021) pkaa076. https://doi.org/10.1093/JNCICS/PKAA076.

[5] G. Ioele, M. Chieffallo, M.A. Occhiuzzi, M. De Luca, A. Garofalo, G. Ragno, F. Grande, Anticancer Drugs: Recent Strategies to Improve Stability Profile, Pharmacokinetic and Pharmacodynamic Properties, Molecules 27 (2022) 5436. https://doi.org/10.3390/molecules27175436.

[6] R.A. Ward, S. Fawell, N. Floc, V. Flemington, D. Mckerrecher, P.D. Smith, Challenges and Opportunities in Cancer Drug Resistance, Chem. Rev. 121 (2021) 3297–3351. https://doi.org/10.1021/acs.chemrev.0c00383.

[7] D. Jurkovicova, C.M. Neophytou, A. ˇCipak Gašparovi´c, A.C. Gonçalves, DNA Damage Response in Cancer Therapy and Resistance : Challenges and Opportunities, Int. J. Mol. Sci. 23 (2022) 14672.

[8] B. Cheng, W. Pan, Y. Xing, Y. Xiao, J. Chen, Z. Xu, Recent advances in DDR ( DNA damage response) inhibitors for cancer therapy, Eur. J. Med. Chem. 230 (2022) 114109. https://doi.org/10.1016/j.ejmech.2022.114109.

[9] W. Choi, E.S. Lee, Therapeutic Targeting of DNA Damage Response in Cancer, Int. J. Mol. Sci. 23 (2022) 1701.

[10] G. Danovski, G. Panova, B. Keister, R. Stamatov, P. Kanev, R. Aleksandrov, K.B. Blagoev, S.S. Stoynov, Diffusion of activated ATM explains gH2AX and MDC1 spread beyond the DNA damage site, ISCIENCE 27 (2024) 110826. https://doi.org/10.1016/j.isci.2024.110826.

[11] S.E. Ruff, S.K. Logan, M.J. Garabedian, T.T. Huang, Roles for MDC1 in cancer development and treatment, DNA Repair (Amst). 95 (2020) 102948. https://doi.org/10.1016/j.dnarep.2020.102948.

[12] I. Dikic, T. Johansen, V. Kirkin, Selective autophagy in cancer development and therapy, Cancer Res. 70 (2010) 3431–3434. https://doi.org/10.1158/0008-5472.CAN-09-4027.

[13] K. Yamamoto, A. Venida, R.M. Perera, A.C. Kimmelman, Selective autophagy of MHC-I promotes immune evasion of pancreatic cancer, Autophagy 16 (2020) 1524–1525. https://doi.org/10.1080/15548627.2020.1769973.

[14] Y. Liu, L. Yu, BRCA1 : a key player at multiple stages of homologous recombination in DNA double - strand break repair, Genome Instab. Dis. 2 (2021) 164–174. https://doi.org/10.1007/s42764-021-00042-1.

[15] X. Li, L. Zou, BRCAness , DNA gaps , and gain and loss of PARP inhibitor – induced synthetic lethality, J. Clin. Invest. 134 (2024) e181062.

[16] P. Moudry, K. Watanabe, K.M. Wolanin, J. Bartkova, I.E. Wassing, S. Watanabe, R. Strauss, R.T. Pedersen, V.H. Oestergaard, M. Lisby, M. Andújar-Sánchez, A. Maya-Mendoza, F. Esashi, J. Lukas, J. Bartek, TOP BP1 regulates RAD51 phosphorylation and chromatin loading and determines PARP inhibitor sensitivity, J. Cell Biol. 212 (2016) 281–288. https://doi.org/10.1083/jcb.201507042.

[17] Z. Yan, X. Ge, J. Wang, F. Xu, M. Li, X. Liu, X. Yu, C. Wu, The impact of TOPBP1 mutations in human cancers on the DNA damage response, Genome Instab. Dis. 3 (2022) 144–162. https://doi.org/10.1007/s42764-022-00072-3.



This open-access article distributed under the terms of the Creative Commons Attribution Non Commercial 4.0 License (CC BY-NC 4.0). To view a copy of this license, visit http://creativecommons.org/licenses/by/4.0

[18] X. Xu, S. Vaithiyalingam, G.G. Glick, D.A. Mordes, W.J. Chazin, D. Cortez, The Basic Cleft of RPA70N Binds Multiple Checkpoint Proteins , Including RAD9 , To Regulate ATR Signaling, Mol. Cell. Biol. 28 (2008) 7345–7353. https://doi.org/10.1128/MCB.01079-08.

[19] M.D. Feldkamp, A.O. Frank, J.P. Kennedy, J.D. Patrone, B. Vangamudi, A.G. Waterson, S.W. Fesik, W.J. Chazin, Surface Reengineering of RPA70N Enables Cocrystallization with an Inhibitor of the Replication Protein A Interaction Motif of ATR Interacting Protein, Biochemistry 52 (2013) 6515–6524.

[20] M. Huang, J. Lu, J. Ding, Natural Products in Cancer Therapy : Past , Present and Future, Nat. Products Bioprospect. 11 (2021) 5–13. https://doi.org/10.1007/s13659-020-00293-7.

[21] S. Ghosh, S.K. Das, K. Sinha, B. Ghosh, K. Sen, N. Ghosh, P.C. Sil, The Emerging Role of Natural Products in Cancer Treatment, Springer Berlin Heidelberg, 2024. https://doi.org/10.1007/s00204-024-03786-3.

[22] R. Pavithra, M.R. Khan, M.S. Khan, Recent advancements in natural compounds for cancer therapy and prevention, Phytochem. Rev. 23 (2024) 1835–1859. https://doi.org/10.1007/s11101-024-09940-0.

[23] J. Chen, L. Zhou, X. Li, X. Wu, Y. Li, L. Si, Y. Deng, Protective effect of zerumbone on sepsis - induced acute lung injury through anti - inflammatory and antioxidative activity via NF - κB pathway inhibition and HO - 1 activation, Naunyn. Schmiedebergs. Arch. Pharmacol. 397 (2024) 2241–2255. https://doi.org/10.1007/s00210-023-02706-z.

[24] M.D. Ibáñez, N.M. Sánchez-Ballester, M.A. Blázquez, Healthy Zerumbone : From Natural Sources to Strategies to Improve Its Bioavailability and Oral Administration, Plants 12 (2023).

[25] H.M. AbuZahra, P. Rajendran, M.B. Ismail, Zerumbone Exhibit Protective Effect against Zearalenone Induced Toxicity via Ameliorating Inflammation and Oxidative Stress Induced Apoptosis, Antibiotics 10 (2021) 1593.

[26] A. Soroush, S. Pourhossein, D. Hosseingholizadeh, A. Hjazi, R. Shahhosseini, H. Kavoosi, N. Kermanshahi, P. Behnamrad, N. Ghavamikia, M. Dadashpour, S.K. Shayan, Anti - cancer potential of zerumbone in cancer and glioma : current trends and future perspectives, Med. Oncol. 41 (2024) 1–14. https://doi.org/10.1007/s12032-024-02327-3.

[27] A. Ostadi, M.M. Vahedi, F. Abbasinezhad-moud, Y. Metanat, F.Q.M. Seraj, A.R. Afshari, S.S. Ahmadi, G.A. Ferns, A. Bahrami, Zerumbone Induces Apoptosis and Inhibits Migration of A2058 Melanoma stem-like Cells by Producing Reactive Oxygen Species , Causing G2 / M Cell Cycle Arrest , and Controlling the Expression of Genes Linked to Metastasis, Indian J. Clin. Biochem. (2024). https://doi.org/10.1007/s12291-024-01260-6.

[28] A. Sehrawat, K. Sakao, S. V. Singh, Notch2 activation is protective against anticancer effects of zerumbone in human breast cancer cells, Breast Cancer Res. Treat. 146 (2015) 543–555. https://doi.org/10.1007/s10549-014-3059-7.

[29] M. Jeon, J. Han, S.J. Nam, J.E. Lee, S. Kim, Elevated IL-1β expression induces invasiveness of triple negative breast cancer cells and is suppressed by zerumbone, Chem. Biol. Interact. 258 (2016) 126–133. https://doi.org/10.1016/j.cbi.2016.08.021.

[30] J. Han, S.Y. Bae, S.J. Oh, J. Lee, J.H. Lee, H.C. Lee, S.K. Lee, W.H. Kil, S.W. Kim, S.J. Nam, S. Kim, J.E. Lee, Zerumbone suppresses IL-1β-induced cell migration and invasion by inhibiting IL-8 and MMP-3 expression in human triple-negative breast cancer cells, Phyther. Res. 28 (2014) 1654–1660. https://doi.org/10.1002/ptr.5178.

[31] A. Sehrawat, J.A. Arlotti, A. Murakami, S. V. Singh, Zerumbone causes Bax and Bak-mediated apoptosis in human breast cancer cells and inhibits orthotopic xenograft growth in vivo, Breast Cancer Res. Treat. 136 (2013) 429–441. https://doi.org/10.1007/s10549-012-2280-5.

[32] B. Sung, S. Jhurani, S.A. Kwang, Y. Mastuo, T. Yi, S. Guha, M. Liu, B.B. Aggarwal, Zerumbone down-regulates chemokine receptor CXCR4 expression leading to inhibition of CXCL12-induced invasion of breast and pancreatic tumor cells, Cancer Res. 68 (2008) 8938–8944. https://doi.org/10.1158/0008-5472.CAN-08-2155.

[33] S. Kim, J. Lee, M. Jeon, J.E. Lee, S.J. Nam, Zerumbone suppresses the motility and tumorigenecity of triple negative breast cancer cells via the inhibition of TGF-β1 signaling pathway, Oncotarget 7 (2016) 1544–1558. https://doi.org/10.18632/oncotarget.6441.

[34] P.K. Chiang, W.K. Tsai, M. Chen, W.R. Lin, Y.C. Chow, C.C. Lee, J.M. Hsu, Y.J. Chen, Zerumbone Regulates DNA Repair Responding to Ionizing Radiation and Enhances Radiosensitivity of Human Prostatic Cancer Cells, Integr. Cancer Ther. 17 (2018) 292–298. https://doi.org/10.1177/1534735417712008.

[35] V. Zarezade, Z. Nazeri, S. Azizidoost, M. Cheraghzadeh, H. Babaahmadi-Rezaei, A. Kheirollah, Paradoxical effect of Aβ on protein levels of ABCA1 in astrocytes, microglia, and neurons isolated from C57BL/6

This open-access article distributed under the terms of the Creative Commons Attribution Non Commercial 4.0 License (CC BY-NC 4.0). To view a copy of this license, visit http://creativecommons.org/licenses/by/4.0/

mice: an in vitro and in silico study to elucidate the effect of Aβ on ABCA1 in the brain cells, J. Biomol. Struct. Dyn. 42 (2024) 274–287. https://doi.org/10.1080/07391102.2023.2201835.

[36] M. Yazdi, M. Hasanzadeh Kafshgari, F. Khademi Moghadam, V. Zarezade, R. Oellinger, M. Khosravi, S. Haas, C.C. Hoch, A.G. Pockley, E. Wagner, B. Wollenberg, G. Multhoff, A. Bashiri Dezfouli, Crosstalk Between NK Cell Receptors and Tumor Membrane Hsp70-Derived Peptide: A Combined Computational and Experimental Study, Adv. Sci. 11 (2024) 1–15. https://doi.org/10.1002/advs.202305998.

[37] K.S. McPherson, D.M. Korzhnev, Targeting protein-protein interactions in the DNA damage response pathways for cancer chemotherapy, RSC Chem. Biol. 2 (2021) 1167–1195. https://doi.org/10.1039/d1cb00101a.

[38] S.P. Singh, K. Nongalleima, N.I. Singh, W.K. Chanu, T.R. Singh, C.B. Singh, Computational Investigation of Zerumbone as an Inhibitor of TNF-alpha Using Molecular Dynamics and Molecular Docking Methods, Lett. Drug Des. Discov. 18 (2020) 258–268. https://doi.org/10.2174/1570180817999201110112221.

[39] S.P. Singh, N.I. Singh, K. Nongalleima, P. Doley, C.B. Singh, D. Sahoo, Molecular docking, MD simulation, DFT and ADME-toxicity study on analogs of zerumbone against IKK-β enzyme as anti-cancer agents, Netw. Model. Anal. Heal. Informatics Bioinforma. 7 (2018) 1–8. https://doi.org/10.1007/s13721-018-0171-3.

[40] E.E.M. Eid, F. Azam, M. Hassan, I.M. Taban, M.A. Halim, Zerumbone binding to estrogen receptors: An in-silico investigation, J. Recept. Signal Transduct. 38 (2018) 342–351. https://doi.org/10.1080/10799893.2018.1531886.

[41] S. Kim, J. Chen, T. Cheng, A. Gindulyte, J. He, S. He, Q. Li, B.A. Shoemaker, P.A. Thiessen, B. Yu, L. Zaslavsky, J. Zhang, E.E. Bolton, PubChem 2023 update, Nucleic Acids Res. 51 (2023) D1373–D1380. https://doi.org/10.1093/nar/gkac956.

[42] J. Eberhardt, D. Santos-Martins, A.F. Tillack, S. Forli, AutoDock Vina 1.2.0: New Docking Methods, Expanded Force Field, and Python Bindings, J. Chem. Inf. Model. 61 (2021) 3891–3898. https://doi.org/10.1021/acs.jcim.1c00203.

[43] E.F. Pettersen, T.D. Goddard, C.C. Huang, G.S. Couch, D.M. Greenblatt, E.C. Meng, T.E. Ferrin, UCSF Chimera - A visualization system for exploratory research and analysis, J. Comput. Chem. 25 (2004) 1605–1612. https://doi.org/10.1002/jcc.20084.

[44] M.J. Abraham, T. Murtola, R. Schulz, S. Páll, J.C. Smith, B. Hess, E. Lindah, Gromacs: High performance molecular simulations through multi-level parallelism from laptops to supercomputers, SoftwareX 1–2 (2015) 19–25. https://doi.org/10.1016/j.softx.2015.06.001.

[45] S.A. Showalter, R. Brüschweiler, Validation of molecular dynamics simulations of biomolecules using NMR spin relaxation as benchmarks: Application to the AMBER99SB force field, J. Chem. Theory Comput. 3 (2007) 961–975. https://doi.org/10.1021/ct7000045.

[46] J. Wang, W. Wang, P.A. Kollman, D.A. Case, Automatic atom type and bond type perception in molecular mechanical calculations, J. Mol. Graph. Model. 25 (2006) 247–260. https://doi.org/10.1016/j.jmgm.2005.12.005.

[47] A. Jakalian, D.B. Jack, C.I. Bayly, Fast, efficient generation of high-quality atomic charges. AM1-BCC model: II. Parameterization and validation, J. Comput. Chem. 23 (2002) 1623–1641. https://doi.org/10.1002/jcc.10128.

[48] J. Zielkiewicz, Structural properties of water: Comparison of the SPC, SPCE, TIP4P, and TIP5P models of water, J. Chem. Phys. 123 (2005). https://doi.org/10.1063/1.2018637.

[49] E.J. Haug, J.S. Arora, K. Matsui, A steepest-descent method for optimization of mechanical systems, J. Optim. Theory Appl. 19 (1976) 401–424. https://doi.org/10.1007/BF00941484.

[50] H.J.C. Berendsen, J.P.M. Postma, W.F. Van Gunsteren, A. Dinola, J.R. Haak, Molecular dynamics with coupling to an external bath, J. Chem. Phys. 81 (1984) 3684–3690. https://doi.org/10.1063/1.448118.

[51] M. Parrinello, A. Rahman, Polymorphic transitions in single crystals: A new molecular dynamics method, J. Appl. Phys. 52 (1981) 7182–7190. https://doi.org/10.1063/1.328693.

[52] S. Miyamoto, P.A. Kollman, Settle: An analytical version of the SHAKE and RATTLE algorithm for rigid water models, J. Comput. Chem. 13 (1992) 952–962. https://doi.org/10.1002/jcc.540130805.

[53] B. Hess, H. Bekker, H.J.C. Berendsen, J.G.E.M. Fraaije, LINCS: A Linear Constraint Solver for molecular simulations, J. Comput. Chem. 18 (1997) 1463–1472. https://doi.org/10.1002/(SICI)1096-987X(199709)18:12<1463::AID-JCC4>3.0.CO;2-H.

[54] T. Darden, D. York, L. Pedersen, Particle mesh Ewald: An N·log(N) method for Ewald sums in large systems, J. Chem. Phys. 98 (1993) 10089–10092. https://doi.org/10.1063/1.464397.



This open-access article distributed under the terms of the Creative Commons Attribution Non Commercial 4.0 License (CC BY-NC 4.0). To view a copy of this license, visit http://creativecommons.org/licenses/by/4.0

[55] J. Lenhard, S. Stephan, H. Hasse, On the History of the Lennard-Jones Potential, Ann. Phys. 536 (2024) 1–4. https://doi.org/10.1002/andp.202400115.

[56] W. Humphrey, A. Dalke, K. Schulten, VMD: Visual molecular dynamics, J. Mol. Graph. 14 (1996) 33–38. https://doi.org/10.1016/0263-7855(96)00018-5.

[57] M.S. Valdés-Tresanco, M.E. Valdés-Tresanco, P.A. Valiente, E. Moreno, Gmx_MMPBSA: A New Tool to Perform End-State Free Energy Calculations with GROMACS, J. Chem. Theory Comput. 17 (2021) 6281–6291. https://doi.org/10.1021/acs.jctc.1c00645.

[58] N. Nezhad, S.S. Saleem, O. Michael, C. Haznie, A. Che, A. Bazli, Evolutionary clade-guided consensus redesign of Is PETase : A computational framework for enhancing thermodynamic stability and MM / PBSA-derived binding energetics, Comput. Biol. Chem. 124 (2026) 109139. https://doi.org/10.1016/j.compbiolchem.2026.109139.

[59] R. Ferreira De Freitas, M. Schapira, A systematic analysis of atomic protein-ligand interactions in the PDB, Medchemcomm 8 (2017) 1970–1981. https://doi.org/10.1039/c7md00381a.

[60] J. Biswal, P. Jayaprakash, R. Rangaswamy, J. Jeyakanthan, Synergistic Effects of Hydration Sites in Protein Stability: A Theoretical Water Thermodynamics Approach, Front. Protein Struct. Funct. Dyn. (2020) 187–212. https://doi.org/10.1007/978-981-15-5530-5_8.

[61] S.P. Singh, K. Nongalleima, N.I. Singh, P. Doley, C.B. Singh, T.R. Singh, D. Sahoo, Zerumbone reduces proliferation of HCT116 colon cancer cells by inhibition of TNF-alpha, Sci. Rep. 8 (2018) 1–11. https://doi.org/10.1038/s41598-018-22362-1.

[62] N.G. Nezhad, A. Eskandari, O.F. Omotayo, S.H. Albayati, S.B. Buhari, T.C. Leow, In Silico Structural Insights into a Glucanase from *Clostridium perfringens* and Prediction of Structural Stability Improvement Through Hydrophobic Interaction Network and Aromatic Interaction, Mol. Biotechnol. 68 (2025) 187–199. https://doi.org/10.1007/s12033-025-01371-2.

[63] N.G. Nezhad, S.B. Buhari, A. Eskandari, S.H. Albayati, O.F. Omotayo, T.C. Leow, Improving the thermostability and substrate affinity of IsPETase through the S209H mutation, and exploring the structural role of the N-terminal: a computational study, 3 Biotech 15 (2025). https://doi.org/10.1007/s13205-025-04258-w.

[64] N.G. Nezhad, M.Y. Borzehandani, A. Eskandari, R.N.Z.R.A. Rahman, N.M. Yahaya, S.N. Oslan, F.M. Shariff, A.L.T. Chor, A comparative investigation of predicted protein structures of a histidine acid phosphatase from Saccharomyces cerevisiae through molecular docking and MD simulations, J. Proteins Proteomics 16 (2025) 35–47. https://doi.org/10.1007/s42485-025-00174-y.

[65] N.G. Nezhad, R.N.Z. Abd Rahman, Y.M. Normi, S.N. Oslan, F.M. Shariff, T.C. Leow, Recent advances in simultaneous thermostability-activity improvement of industrial enzymes through structure modification, Int. J. Biol. Macromol. 232 (2023) 123440. https://doi.org/10.1016/j.ijbiomac.2023.123440.

[66] N.G. Nezhad, R.N.Z. Abd Rahman, Y.M. Normi, S.N. Oslan, F.M. Shariff, T.C. Leow, Thermostability engineering of industrial enzymes through structure modification, Appl. Microbiol. Biotechnol. 106 (2022) 4845–4866. https://doi.org/10.1007/s00253-022-12067-x.

[67] S.B. Buhari, N.G. Nezhad, Y.M. Normi, F.M. Sharif, T.C. Leow, Homology modeling and thermostability enhancement of Vibrio palustris PETase via hydrophobic interactions, J. Biomol. Struct. Dyn. (2025) 1–14. https://doi.org/10.1080/07391102.2024.2440646.

[68] N. Rana, P. Solanki, R. Mehra, A. Manhas, Identification of natural compound inhibitors for substrate-binding site of MTHFD2 enzyme: Insights from structure-based drug design and biomolecular simulations, Chem. Phys. Impact 10 (2025) 100809. https://doi.org/10.1016/j.chphi.2024.100809.

This open-access article distributed under the terms of the Creative Commons Attribution Non Commercial 4.0 License (CC BY-NC 4.0). To view a copy of this license, visit http://creativecommons.org/licenses/by/4.0/